Absorber tube displacement in parabolic trough collectors – A review and presentation of an airborne measurement approach

C. Prahl [a,*], M. Röger [a], B. Stanicki [b], C. Hilgert [a]

[a] Deutsches Zentrum für Luft- und Raumfahrt e.V. (DLR), Institute of Solar Research, Ctra. de Senes s/n, 04200 Tabernas, Spain
[b] Hochschule Ravensburg-Weingarten, 88241 Weingarten, Germany

ABSTRACT

Parabolic trough collectors for concentrating solar sower plants are large scale optical devices with demanding requirements on optical and mechanical properties. Accurate mirror shape and absorber tube alignment are necessary to harness solar radiation with high efficiency. There are several methods to assess the shape of the mirror surface, yet there exist few approaches to effectively measure the position of the absorber tube. This paper provides a comprehensive overview on causes and effects of absorber tube displacement and on state of the art measurement techniques. A new approach on fully automated airborne absorber tube position measurement for parabolic trough collectors is presented, which outperforms existing methods concerning speed, spatial resolution, and level of automation, thereby achieving an accuracy of about 1.5 mm in vertical and lateral direction.

1. Introduction

The terms Concentrating Solar Power (CSP) or Solar Thermal Energy (STE) cover all methods where solar radiation is concentrated by lens- or mirror arrays before harnessing the thermal energy of the sun light. Among the different systems which are commercially available (Irena, 2013), the Parabolic Trough Collector (PTC) is considered the most mature technology with 4.2 Gigawatt (GW) installed capacity worldwide (CSP-Today, 2017). PTCs (Price et al., 2002; Fernandez-Garcia et al., 2010) are high precision optical devices, and the optical and mechanical properties of the concentrator and the Receiver tube (aka.: **H**eat **C**ollecting **E**lement) (HCE) are crucial for the efficiency of the power plant.

The optical performance depends to a large extend on the geometric accuracy of the concentrator. This share is commonly described by the Intercept Factor (γ), which is the ratio of irradiation hitting the absorber and reflected irradiation from the concentrator following the definition of Bendt et al. (1979, p. 9). Three independent geometrical properties determining the γ can be distinguished (Bendt et al., 1979; Pottler et al., 2014).

1. The shape accuracy of the mirror surface is commonly represented by slope deviations of the mirror from the design shape (Slope deviation in curvature direction (SD_X) and Slope deviation in longitudinal direction (SD_Y)). Mirror shape accuracy is considered to be the most important property for any CSP concentrator. It depends on the compliance with tolerances of the concentrator components (e.g. mirrors and structure), on the assembly accuracy and the concentrator's capabilities to withstand gravitational loads. A state of the art review on methods to determine the shape and/or slope deviations of CSP concentrators is presented in Ren (2014).
2. Tracking accuracy describes the deviation between the optical axis of the concentrator and the sun position, projected on the XZ plane of the concentrator (Bendt et al., 1979, Sec. 2.1, Fig. 2.1). Assuming a correct operation of the tracking system (mechanics, sun position algorithm, and optional sun-sensors), the local direction of the optical axis along the trough may be altered by wind, static unbalance and bearing friction. Such torsion effects are best assessed by means of inclinometers (Pottler et al., 2014).
3. This paper focuses on Absorber tube displacement along the optical axis (ΔZ_{Abs}) and Absorber tube displacement in lateral direction (ΔX_{Abs}). In all operation conditions, the absorber tube center line is supposed to be co-axial with the PTCs focal line.

There are several ways to estimate the impact of geometrical deviations on the γ. The statistical Ray Tracing (RT) approach presented in Bendt et al. (1979) consist of folding the sunshape with additional statistical concentrator errors, that way generating an

* Corresponding author.
E-mail address: christoph.prahl@dlr.de (C. Prahl).
URL: http://www.dlr.de/sf/en/desktopdefault.aspx (C. Prahl).

<div style="border:1px solid black">

Nomenclature

Abbreviations

CSP	Concentrating Solar Power
CSR	Circumsolar Ratio: (Buie and Monger, 2004)
DLR	Deutsches Zentrum für Luft- und Raumfahrt e.V.
DNI	Direct Normal Irradiance [W/m^2]
DSG	Direct Steam Generation
EOR	Exterior Orientation: camera positions obtained by photogrammetric evaluation (Luhmann et al., 2006)
ET	EuroTrough Collector (Geyer et al., 2002)
FEP	Front End Plate: end face of Parabolic Trough Collector (PTC) steel structure orientated towards the drive pylon
GUI	**G**raphical **U**ser **I**nterface
GW	Gigawatt
HCE	Receiver tube (aka.: **H**eat **C**ollecting **E**lement)
HTF	Heat Transfer Fluid: see (Vignarooban et al., 2015)
IOR	Interior Orientation: Set of parameters describing the internal geometry and lens distortion of the camera (Luhmann et al., 2006)
KONTAS	Concentrator Test Bench at PSA, Almeria, Spain
LOS	Line-of-Sight
MATLAB	**MA**trix **LAB**oratory: proprietary programming language developed by MathWorks
NREL	National Renewable Energy Laboratory
PG	Close Range Photogrammetry
POI	Point of Interest
PSA	Plataforma Solar de Almería, Spain
PTC	Parabolic Trough Collector
PV	Photovoltaics
QFly	Airborne Qualification of CSP Plants
REP	Rear End Plate
REPA	**R**otation and **E**xpansion **P**erforming **A**ssembly: flexible tube connector or ball joint to link HCE with solar field header

ROI	Region of Interest
RP3	PTC Mirror quasi standard with 1710 mm focal length and 5774 mm aperture width
RT	Ray Tracing
SCA	Solar Collector Assembly
SCE	Solar Collector Element
SPRAY	**S**olar **P**ower **RAY**tracing Tool (Buck, 2010)
STE	Solar Thermal Energy (same as CSP)
STRAL	**S**olar **T**ower **RA**y tracing **L**aboratory (Belhomme et al., 2009)
TARMES	**T**rough **A**bsorber**R**eflection **ME**asurment **S**ystem
UAV	Unmanned Aerial Vehicle
WP	Waypoint of UAV flight route

Mathematical symbols and units

f	focal length
ΔX_{Abs}	absorber tube displacement in lateral direction
ΔZ_{Abs}	absorber tube displacement along the optical axis
γ	intercept factor: ratio of solar irradiation hitting the receiver versus irradiation reflected from the concentrator, when ρ_{Ref}, τ_{Glass}, and α_{Rec} were equal to 1 (Bendt et al., 1979)
SD_X	slope deviation in curvature direction
SD_Y	slope deviation in longitudinal direction
T_{HTF}	Heat Transfer Fluid (HTF) temperature
θ	PTC tracking angle: 90° corresponds to zenith
ρ_{Ref}	specular mirror reflectivity
τ_{Glass}	glass envelope tube transmissivity
α_{Rec}	absorber tube absorptivity

</div>

"effective" source with a wider angle distribution compared to the initial sunshape. Applications of statistical RT to PTC fields are presented among others in Lüpfert et al. (2007) and Pottler et al. (2014). A brief explanation on advantages and drawbacks of this method can be found in Zhu and Lewandowski (2012, Sec. 2.2.2).

An extensive analytical approach to determine the flux incident on an absorber tube considering statistical concentrator errors and a bent tube is presented in Khanna et al. (2013, 2014, 2015). An analytical approach called FirstOPTIC, which preserves the spatial information of shape- and absorber tube deviations while employing a probability approximation from Bendt et al. (1979) for the sun-shape was developed by Zhu and Lewandowski, 2012 and Binotti et al. (2012).

Numerical RT is the state of the art approach to assess the optical performance of CSP systems. Based on measured concentrator geometry, RT predicts the optical performance correctly even for cases where systematic deviations are present. RT simulations consider blocking and shading elements[1] which interfere with incident and reflected radiation. A current review on available RT tools and their abilities is available in Ho (2008) and Bode and Gauche (2012).

Absorber tube displacement may effect both the optical performance of the concentrator as well as the result of optical measurement techniques using the absorber tube position as an input parameter. This article was motivated by the development of Airborne Qualification of CSP Plants (QFly) (Prahl et al., 2011, 2013; Stanicki, 2011), where slope deviations of PTC solar fields are characterized by the **T**rough **A**bsorber**R**eflection **ME**asurment **S**ystem

(TARMES) (Ulmer et al., 2009) approach, which in turn is based on the distant observer technique proposed by Wood (1981). For this approach, the absorber tube serves as a pattern. The absorber reflection visible in the mirror is used to deduce the mirror shape. Therefore it was necessary to develop a method suited to simultaneously measuring the absorber tube position along with mirror shape deviations. In addition, a reasonable statement on the optical performance by means of RT is only possible if the entire geometry is known with sufficient spatial resolution and accuracy.

Section 2 of this article describes the cause and effect of absorber tube displacement as well as applications of absorber position data. In Section 3, an overview on state-of-the-art methods to measure the absorber tube deviations is given. In Section 4, a new airborne approach for absorber tube positioning suited for large number of collectors is introduced and validated against a high-precision photogrammetric benchmark measurement. The results and further suggestions are discussed in Section 5.

2. Absorber tube displacement

The thermal energy absorbed by the HCE is transferred to a Heat Transfer Fluid (HTF) circulated inside the stainless steel tube with typical diameter in the range of 70–90 mm (Schott, 2015b,a). All HCEs designed for high temperature applications are surrounded by an evacuated glass envelope tube with an anti-reflective coating to minimize convection heat losses and to maximize the transmittance. A spectral selective coating of the steel tube assures high absorptivity an low radiative heat losses. The cost share of the HCEs is about 7% of the total investment cost of the entire plant

---

[1] Bellow protections and receivers supports.

(WorldBank, 2010, page 75, table 8). Thus, HCEs can be regarded as a sensitive key component. In order to harness its full performance, the deviation of the tube center line from the focal line ($\Delta X_{Abs}/\Delta Z_{Abs}$) must not exceed the specified tolerances (see Fig. 4).

2.1. Causes for absorber tube displacement

2.1.1. Mounting precision

Absorber tubes are connected to the PTC structure via supports, which keep the tube in a position coaxial with the focal line during tracking. The supports are connected to the concentrator structure via a link or spring plate close to the parabola vertex which allows for motion in longitudinal direction in order to compensate for the thermal expansion of the tubes between ambient and operation temperature (see Fig. 2).

The state of the art is to assemble the (steel-) structures of PTCs upside-down on carefully adjusted jig (Geyer et al., 2002). This jig comprises the exact locations of mirror mounting points, axis of rotation and the focal line. With these measures, tolerances for the absorber tube supports less than 2 mm can be complied with. In case of a an defective or incorrectly positioned jig, or in the absence of such a device, much larger deviations have been observed.

2.1.2. Thermal stress

Thermal stress caused by inhomogeneous illumination and inadequate heat transfer may cause residual stress and permanent deformation of the steel tube. Modeling of stress and deflection with thermal oil HTF has been investigated, however assumptions and modeled deflections differ significantly from operation experience in commercial plants (Yaghoubi and Akbarimoosavi, 2011). Another critical operating condition is stratified flow (Hirsch et al., 2012) in the absorber tube in combination with inhomogeneous radiation distribution or instabilities (phase changes) in Direct Steam Generation (DSG) facilities (Valdes et al., 2014; Almanza et al., 1997). Investigations concerning HCE deformation and the influence on the γ in case of molten salt

HTF antifreeze installations have been reported in Iverson et al. (2011). Here, deflections up to 16.4 mm are reported when hot molten salt flushes the tube. Indoor experiments, numerical simulations and field measurements to investigate the causes of absorber tube bending are presented in Wu et al. (2014). Reported deflections are rather influenced by the mechanical boundary conditions, while HTF temperature and mass flow are of lower relevance. Significant absorber tube deviation between the supports has been observed occasionally before any exposure of the tube to concentrated solar radiation. A common explanation for this phenomenon is an incorrect welding procedure. In order to assure high level quality of the HCE connections during solar field assembly, orbital welding equipment is used.

### 2.1.3. HTF temperature below nominal operation temperature

Structures of parabolic troughs are designed in a way, that the HCE supports are in upright position when the HTF temperature at the outlet T_{HTFout} has reached the nominal operation temperature T_{HTFnom}. As a consequence, the supports are tilted towards the drive for $T_{HTFout} < T_{HTFnom}$, and the absorber tube center line is located below the focal line (see Figs. 2 and 5).

$$\Delta Z_{Abs} = \sqrt{(f-b)^2 - (y \cdot \alpha \cdot \Delta T)^2} - (f-b) \qquad (1)$$

provides an approximation for vertical displacement for small support tilting angles. Here, f is the focal length, b is the distance of the support pivot from vertex, y is the longitudinal distance from drive pylon (fixed point). α denotes the thermal expansion coefficient and $\Delta T = T_{HTFnom} - T_{HTFout}$ is the temperature difference between actual and nominal HTF temperature. Such reversible vertical deviations are part of the normal operation procedure and no long term effect on life time of the plant was reported yet. Effects on the optical performance are presented in Section 2.2 and Fig. 5.

2.1.4. Dead load

Gravitational effects can be divided in sagging of the tube between supports and deformation of the supports and due to dead load in different elevation angles. For the first mentioned,
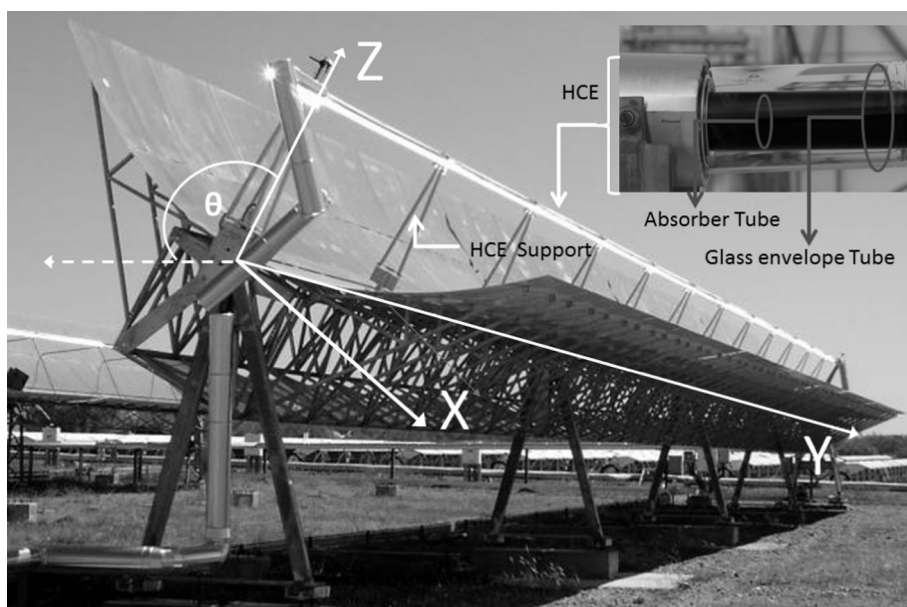
Fig. 1. EuroTrough Collector (ET) PTC SCA at the PSA. The coordinate convention used in this paper is shown as well as the main components of interest. The PTC tracking angle (θ) denotes the angle between the optical axis (Z) and the horizontal. The Y-axis denotes the vertex of the parabolic trough, while the X-axis is perpendicular to Y and Z. The HCE consists of a stainless steel absorber tube surrounded by a glass envelope tube for thermal insulation (Schott, 2015b). The welding connection and the bellow allowing for thermal expansion between the steel absorber tube and the glass envelope tube are protected with an aluminum sheet cylinder.
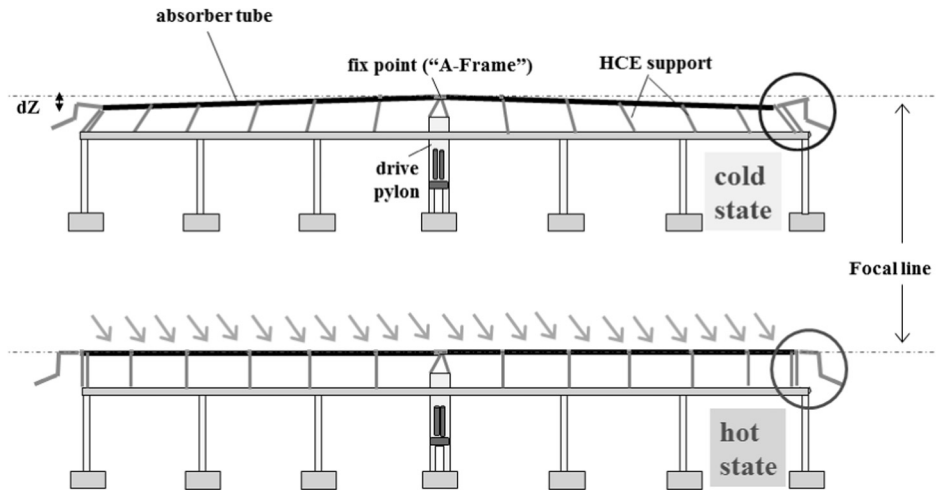
Fig. 2. Sketch of PTC with HCE at ambient temperature (top, cold state) and at operation temperature (bottom, hot state). Thermal expansion is compensated by tilting of the HCE supports, which leads to increasing ΔZ_{Abs} towards the trough ends in the cold state.
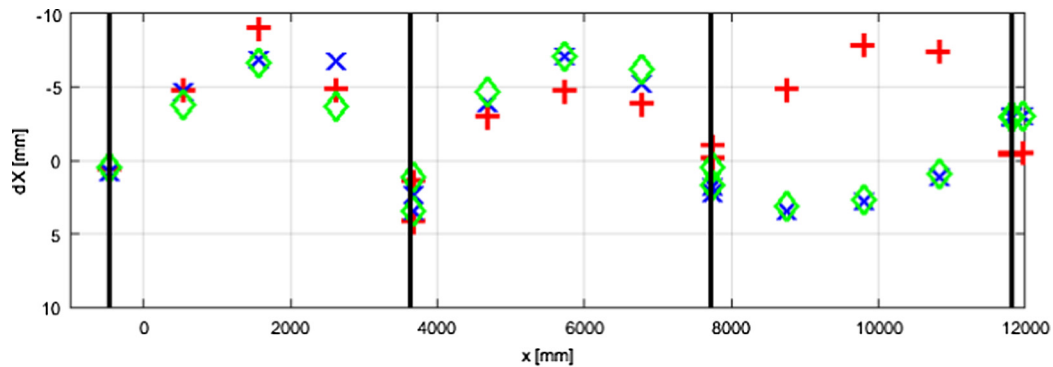
Fig. 3. ΔX_{Abs} measured by the method presented in Section 3.2 for tracking angle θ facing zenith for different rotation directions. For data points represented by $\diamond$ and X, the current elevation position has been approached repeatedly from $\theta > 0°$, while + symbols refer to approaches from the opposite direction. The HCE towards the REP suffers significant deformation due to friction loads from the flexible tube connectors. Towards the FEP deformations are avoided by a more rigid structure.

sagging about 3 mm for empty and 6 mm for tubes filled with molten salt have been reported by Iverson et al. (2011). For the latter effect, dead load M introduces a torque proportional to $\approx M \cdot \sin(\theta) \cdot f$. Dead load induced ΔX_{Abs} due to deflection of the supports should not exceed the range of 5 mm taking into account additional effects like mounting precision, etc. (see Fig. 4). Values for prototypes of up to 30 mm displacement between zenith and horizon position have been reported in Stynes and Ihas (2012a, Sec. 8.3).

2.1.5. Forces and torque from flexible tube connectors

At the outer ends of each SCA, **R**otation and **E**xpansion **P**erforming **A**ssemblys (REPAs) are installed to compensate for the rotation of the collector and thermal expansion of the absorber tube relative to the plant header and cross over pipes. REPAs introduce additional forces and torque, caused by dead load and friction. Such deformations have been quantified[2] at a single ET mounted at the KONTAS (Heller et al., 2011) test facility at PSA. A hysteresis can be observed (see Fig. 3), as friction depends on previous motion direction. The influence on the performance of observed moderate deflections can be neglected in typical solar fields, as only 5% of the HCEs are affected.

---

[2] Using the methods described in Sections 3.2 and 3.3.

### 2.2. Effects of absorber tube deviations

2.2.1. Decrease of optical efficiency

Moderate absorber tube displacement has a minor effect on the optical performance, but as soon as the displacement exceeds a certain collector specific value, the γ is decreased significantly (Lüpfert et al., 2007, Figs. 11 and 12). In some cases, independent geometrical properties compensate each other. Tracking errors may be balanced by $|\Delta X_{Abs}| > 0$ and systematic deviations of the mirror shape from the design focal length may be compensated by $|\Delta Z_{Abs}| > 0$. RT analysis on the sensitivity of the γ for different HCE positions and mirror slope errors is presented in Fig. 4. Detailed investigations on this issue can be found in Schiricke (2008).

Systematic height deviations ($\Delta Z_{Abs} < 0$) caused by $T_{HTFout} < T_{HTFnom}$ (see Section 2.1.3 and Fig. 5) are expected to reduce the γ. Annual performance losses are moderate because significant deflections appears only at the outer end of the collector. Furthermore, this particular operation condition is in general only met at low solar elevation angles, thus times with low Direct Normal Irradiance [W/m²] (DNI). A systematic investigation on this effect for an entire SCA is presented in Fig. 5.

2.2.2. Destruction of glass envelope tube

Commonly used HCEs like the SCHOTT PTR 70 (Schott, 2015a) have an outer diameter of the glass envelope tube of 125 mm with
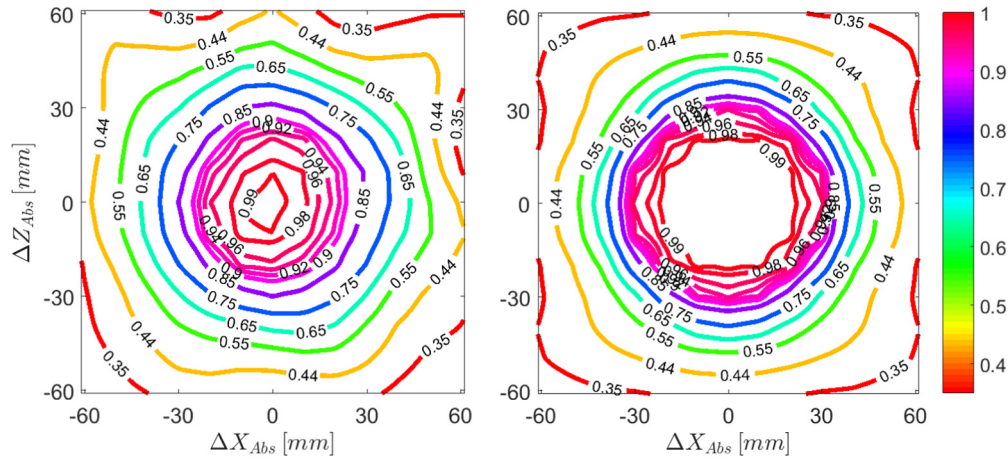
Fig. 4. RT based sensitivity analysis (CSR = 0.05) of the Intercept Factor (γ) for different ΔZ_{Abs} and ΔX_{Abs} combinations and mirror shapes. The left graph shows results for a real RP3 concentrator with an SD_X RMS of 2.1 mrad. The graph on the right side is based on an ideal mirror. For the given rim-angle, ΔZ_{Abs} and ΔX_{Abs} have similar impact and characteristics of γ-decrease also depends on the SD_X RMS. An ideal reflector (right) is less susceptible to absorber tube misalignment, because the narrow "effective source" (Bendt et al., 1979) beam angle of the cone of reflected radiation. The γ has then a larger plateau at its maximum value of 0.99. On the other hand, the wider distribution of the "effective source" of a real collector partly inhibits the quick γ-decrease for larger absorber tube deviations.
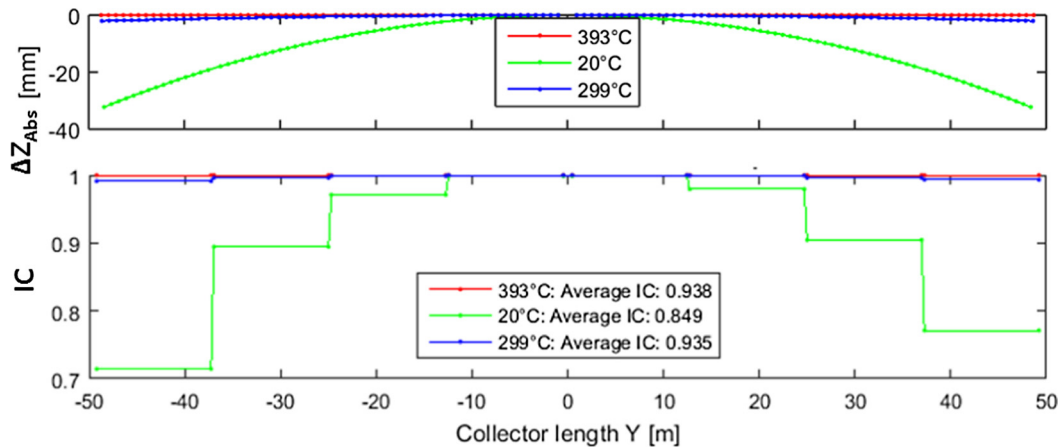
Fig. 5. Top: Thermal expansion induced ΔZ_{Abs} for an ET SCA with four SCEs on each side of the drive pylon for different T_{HTF} ($T_{nominal}$ = 393 °C) under the assumption of vertical HCE supports at nominal T_{HTF}. Bottom: Normalized RT based γ values for different T_{HTF} based on mirror shapes obtained by QFly and ideal absorber position (at nominal temperature). Steps in γ graph are due to the fact that a single scalar γ value is assigned to each 12 m long SCE. Deviations from expected symmetric γ decrease towards the outer ends is caused by individual SD_X characteristics (RMS 3.5–4.5 mrad) of each SCE.

a wall thickness of 3 mm, so bending of the steel tube exceeding 25 mm may destroy the glass tube. Such failures are mainly caused by thermal stress (see Section 2.1.2). Glass tube destruction caused by excessive friction of the REPAs and corresponding steel tube bending (see Section 2.1.5) has also been reported. An overview on field statistics and effects on performance is given in Burkholder and Kutscher (2009).

### 2.2.3. Malfunction of tracking system

Most PTCs use a sun sensor as input for a tracking feedback control. There are various types of sun-sensors for different solar applications (Mousazadeh et al., 2009). In some ET-type PTCs, two Photovoltaics (PV) cells are mounted in the optical plane above the vertex in order to detect the position of the shadow of the absorber tube relative to the parabola vertex (see Fig. 6). Tracking is adjusted until the tube shadow is centered above the vertex, assuming that in this case the incoming radiation is parallel to the optical plane. $|\Delta X_{Abs}| > 0$ will directly lead to tracking error of $\sin(\Delta X_{Abs}/f)$, if such PV-cell based tracking sensors are deployed. Thermal tests at the KONTAS facility showed the sensitivity of this

control concept to tracking angle dependent ΔX_{Abs}. Tracking was optimized by maximizing the thermal output. The parameters of the sun sensor based tracking system had to be adjusted in the course of the day to compensate for ΔX_{Abs} as a function of θ and tracking direction (Nouri, 2014).

2.3. Applications of absorber tube displacement data

The availability of accurate and spatially high resolved absorber tube displacement data offers a variety of applications like optical performance calculation with numerical RT. Another application is the performance optimization by retroactive adjustment of the receiver position. Corrections of PTC structures in the solar field are not foreseen and the effort for such corrections is much higher compared to a proper in-line quality control. Yet, post-production absorber tube alignment in the solar field has been realized with positive impact on the optical performance (Pottler et al., 2014).

The focus of the present work rests on using absorber tube displacement data as input for deflectometric PTCs mirror shape measurement (Ulmer et al., 2009; Diver and Moss, 2007; Jorgensen
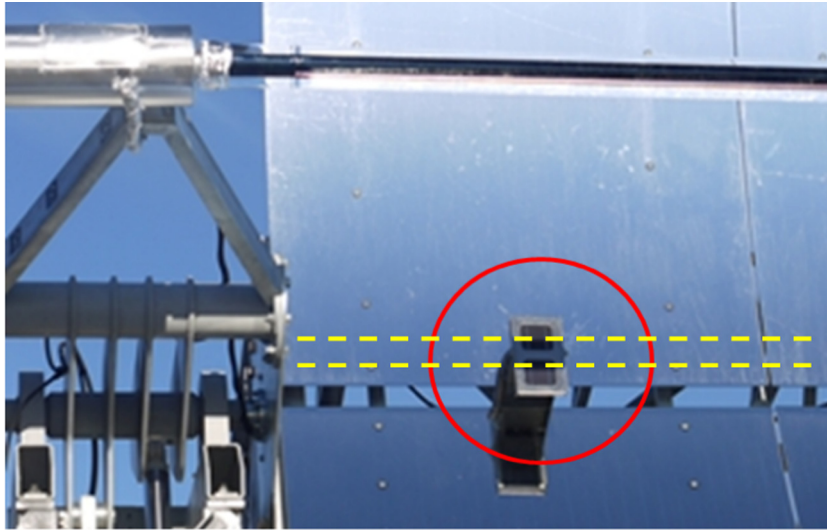
Fig. 6. Absorber tube shadow (dashed lines) casting the PV cell based sun sensor (inside circle). The difference of current signal from both PV cells is used to trigger tracking movements.

et al., 2009; Prahl et al., 2011; Stynes and Ihas, 2012a; Francini et al., 2012). The TARMES method (Ulmer et al., 2009) was recently enhanced from ground based to airborne data acquisition (Prahl et al., 2013) (see Section 4.1). In this context, it became clear that the uncertainty of the absorber tube positioning must not exceed 2–4 mm to achieve the desired mirror shape measurement accuracy. As state of the art methods (see Section 3) are not applicable to large solar fields, the initial approach was to assume that the absorber is located in its design position coaxial with the focal line. SD_X results provided that way would rather represent combined mirror- and absorber deviations.[3] To distinguish between mirror shape and absorber displacement, a new approach to simultaneously measure the absorber position for large fractions of the solar field from aerial images has been developed and will be presented in Section 4.

3. State of the art absorber tube position measurement

State of the art measurement techniques are presented in the following sections. An innovative method proposed by National Renewable Energy Laboratory (NREL) (Stynes and Ihas, 2012a,b) will be discussed in Section 3.5. Beyond that, no further methods have been found in the literature. As direct access to the steel tube is prevented by the glass envelope tube, measurement of $\Delta X / Z_{Abs}$ is in general a two stage process. At first the axis of the glass envelope tube is measured (Sections 3.1 and 3.2) and then the eccentricity of absorber and glass tube is estimated from digital images (Section 3.3). The superposition of glass envelope tube position and eccentricity gives the absolute deviation of the steel tube from the focal line. Another option is to measure only relative absorber tube displacement in one direction by exploiting the information of digital images taken by a camera attached firmly to the collector structure (see Section 3.4).

3.1. Photogrammetric measurement of the glass envelope tube position

Close Range Photogrammetry (PG) Luhmann et al. (2006) is nowadays an established method to determine the shape of CSP collectors Pottler et al. (2004), Fernandez-Reche and Valenzuela

(2012), and Garcis et al. (2012). Point of Interests (POIs) on the mirror surface, the tracking axis and the absorber tube are highlighted with circular, retro-reflective markers. After image acquisitions, 2D image coordinates of the markers are obtained via image processing and 3D position of the POIs are calculated by bundle adjustment. The post-processing of the POI 3D data, which allows for comparison between measured and design coordinates, shall be explained briefly. The POI cloud is provided in an arbitrary orientated coordinate system. A sufficient number of reference points in both the measured data A and the design data B is required to determine the spatial transformation parameters (translation: $c_{x,y,z}$, rotation: $r_{x,y,z}$, scaling: μ), which are used to transform (Eq. (2)) the measurement point cloud into the design data coordinate system.

$$
\begin{bmatrix} X \\ Y \\ Z \end{bmatrix}^B = \begin{bmatrix} c_x \\ c_y \\ c_z \end{bmatrix} + \mu \cdot \begin{bmatrix} 1 & r_z & -r_y \\ -r_z & 1 & r_x \\ r_y & -r_x & 1 \end{bmatrix} \cdot \begin{bmatrix} X \\ Y \\ Z \end{bmatrix}^A \qquad (2)
$$

A common approach to obtain the transformation parameters is a least-squares fit of all mirror POIs to the design data. Another approach of determining the transformation parameters emphasizes the role of the axis of rotation, as described in the following. Translation parameters $c_{x,y,z}$ are determined by moving the origin of the measured data OA to origin of the design data OB. A reasonable definition of the origin is the end of the axis of rotation facing towards the drive pylon (FEP, see Fig. 1). Rotation angles $r_{x,z}$ to align parabola vertex or the axis of rotation of measured and design data are obtained by merging the opposite end of the vertex/axis of rotation (REP). The rotation angle r_y is calculated by minimizing the difference between measured mirror POIs and corresponding design data points. The center of glass envelope tube can be calculated by fitting a circle to the corresponding targets (see Fig. 7).

3.2. Manual measurement of the glass envelope tube position

The previous described photogrammetric approach can hardly be applied to larger numbers of SCEs because it requires substantial preparation efforts. A less precise but much faster approach involves direct distance measurement between the glass envelope

---

[3] The term *reflector-absorber angles* is used in Stynes and Ihas (2012a, page. 31).
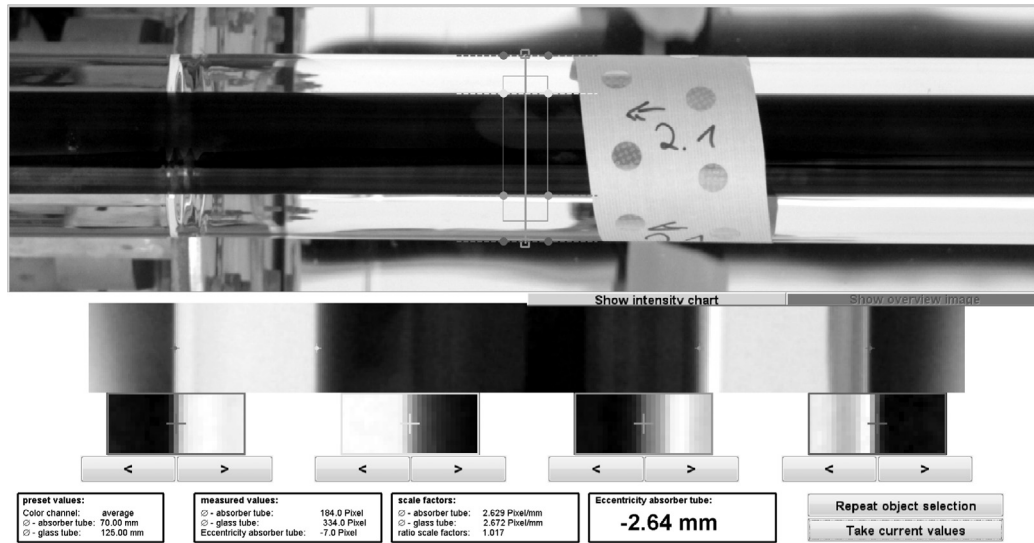
Fig. 7. Methodology of evaluation of eccentricity image with a MATLAB GUI. The upper area shows the enlarged ROI with the absorber tube in front of the vertex of the parabola. Semi-automatic edge based algorithms help to determine the position of glass- and steel tube edges in the cross-section (lower area). The visible paper stripe with retro-reflective targets serves to determine the glass envelope tube position by means of photogrammetry.

tube and the outer mirror edges with a hook rod. The relation between the difference of opposite hook rod measurements d_{Hook} and lateral glass tube displacement ΔX_{Glass} depends on the parabola width x and f given by

$$\Delta X_{Glass} = \frac{d_{Hook}}{2} \cdot \cos\left(\arctan\left(\frac{f - \Delta Z_{Glass} - \frac{x^2}{4 \cdot f}}{x}\right)\right) \qquad (3)$$

ΔZ_{Glass} is obtained from HCE support tilt angles β in Y-direction from digital images with the relation: $\Delta Z_{Glass} = \cos(\beta) \cdot (f - Z_{Pivot})$. Here, Z_{Pivot} is the distance between the support rotation axis and the vertex. This method to determine ΔZ_{Glass} only compensates for the tilt of the supports. It is no control for deviations due to manufacturing inaccuracies. The calculations presented here are based on the assumption of an ideal collector geometry (e.g. outer mirror edges symmetrical with respect to vertex and length of HCE supports fits design criteria).

3.3. Evaluation of eccentricity images

To obtain the eccentricity of the steel absorber tube relative to the glass envelope tube, digital images are semi-automatically evaluated with a MATLAB **G**raphical **U**ser **I**nterface (GUI) (see Fig. 7). To obtain ΔX_{Abs}, images are taken along the optical axis, and for ΔZ_{Abs} perpendicular to the optical axis and vertex. The user has to select Region of Interests (ROIs) in the raw images, and the edges of the steel- and glass tube are calculated from an cross sections perpendicular to the focal line. A similar approach is also presented in Wu et al. (2014).

3.4. Relative measurement from image series

With a camera attached firmly to the collector structure, relative values for ΔX_{Abs} and ΔZ_{Abs} caused by thermal or mechanical stress can be quantified with high temporal- and spatial resolution. For two dimensional characterization at least two cameras are required. Lateral deviations can be monitored with a camera mounted close to the vertex, while hight deviations are best observed with camera mounted close to the mirror edge. Such

measurements have been carried out by Wu et al. (2014), Hirsch et al. (2012), and Iverson et al. (2011).

3.5. NREL absorber alignment measurement tool for PTCs

An absorber alignment measurement technique from NREL (Stynes and Ihas, 2012b,a) uses a photogrammetric approach with additionally attached markers to determine the camera position relative to the PTC. The interior orientation of the camera is acquired by using a calibration toolbox (Bouguet, 2010). The height and lateral deviation of the absorber tube are calculated by solving a system of linear equations including the camera position and the absorber tube projected on a plane parallel to the aperture plane including the focal line. Two or more camera positions with preferred height of 10 m above the parabola vertex are chosen. The uncertainty analysis published in Stynes and Ihas (2012a, Sec. 7.4) predicts values in the range of 5–10 mm. The validation of the method with a manually operated camera and a mock collector/receiver without glass envelope tube showed deviations between the absorber alignment measurement technique and a PG reference measurement in the range of 1.5 mm for ΔX_{Abs} and 0.9 mm for ΔZ_{Abs}.

4. Airborne absorber tube positioning of parabolic troughs

The airborne measurement system QFly (Prahl et al., 2013) was developed to obtain the optical performance for entire PTC solar fields. The position of the HCE is indispensable to characterize the optical performance of PTCs with the TARMES principle. A fully automated approach to measure $\Delta Z_{Abs}/\Delta X_{Abs}$ is presented with an uncertainty analysis and validation against a photogrammetric benchmark. Fig. 8 sketches the QFly work flow and highlights the topic presented in this article.

4.1. System description

The airborne PTC characterization system QFly consist of a commercial available hardware platform[4] and self-developed MATLAB

---

[4] md4-1000 Unmanned Aerial Vehicle (UAV) quadcopter from microdrones.
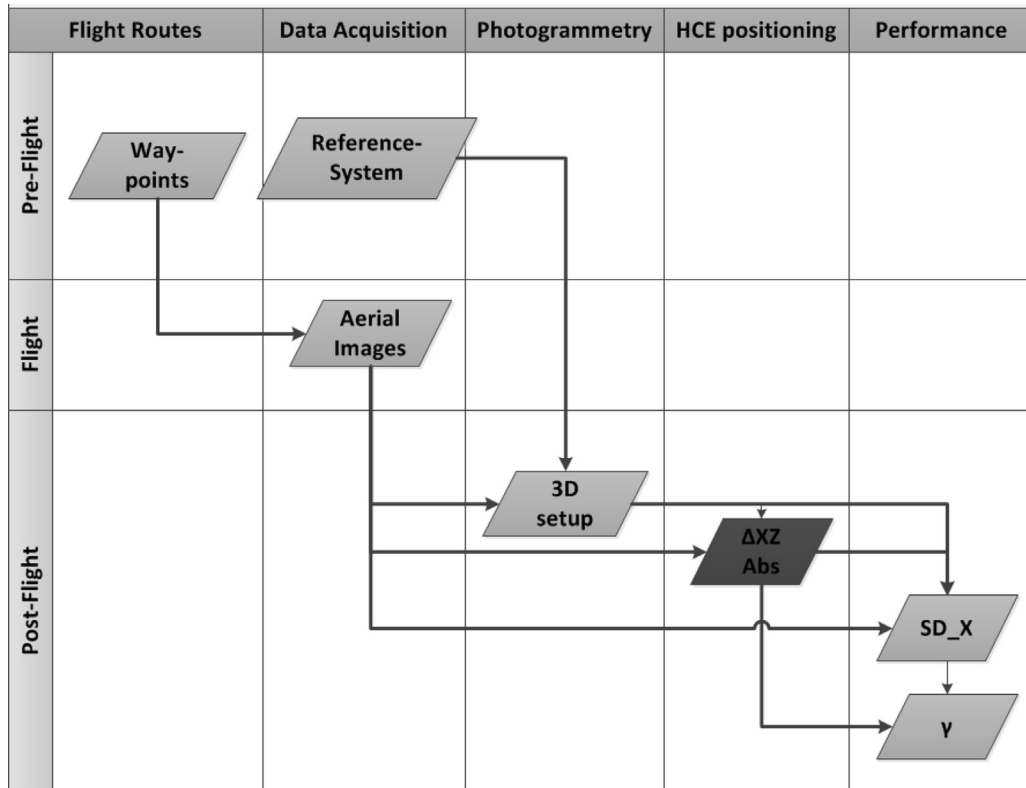
Fig. 8. Methodology and data flow of QFly. The absorber tube deviation (ΔX_{Abs}, ΔZ_{Abs}) is a key parameter which serves for shape- (Slope deviation in curvature direction (SD_X)) and performance (γ) calculation.
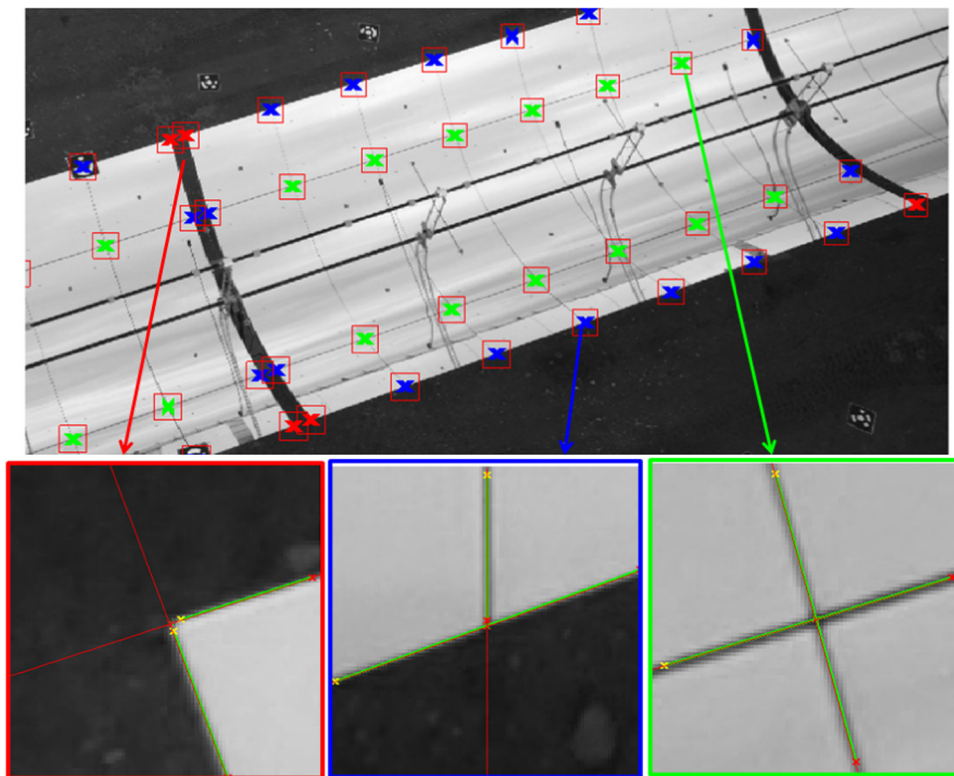
Fig. 9. "Natural" feature of the mirror surface (gap, corners and crosses) are detected by image processing and serve as markers for the photogrammetric evaluation. Hough transformation (Gonzalez et al., 2004) is used to accurately identify mirror edges and vertices.

code for flight route planning and fully automatic evaluation. The camera position is obtained from PG using inherent mirror features as POIs (see Fig. 9). SD_X is calculated from absorber tube reflex images using the TARMES approach. Optical performance is obtained with a RT interface to the software **S**olar **P**ower **RAY**tracing Tool (SPRAY) and **S**olar **T**ower **RA**y tracing **L**aboratory (Belhomme et al., 2009) (STRAL). A detailed description of the hardware an methodology of QFly can be found in Prahl et al. (2013, Sec. 4). A recent change to the hardware compared to former publications is the use of a different camera (Sony Nex 7) with higher frame rate and resolution in order to enhance the data quality and to increase the measurement volume per flight. The automatic flight route was adapted to fulfill the requirements of both TARMES and the HCE positioning by adding a rising and descending path to each SCE flyover (see Fig. 10). The QFly system is currently capable performing the image acquisition for an entire ET SCA in less than 1 h and automatic post processing in less than 3 h, depending on computer performance.

The photogrammetric determination of the camera position relative to each SCE has been improved by using 24 additional mirror features per SCE like crosses and gaps between the panels (see Fig. 9). Artificial coded markers are only required for the first iteration of the photogrammetric evaluation and are planned to be obsolete in future releases.

The following description is based on a coordinate system convention as shown in Fig. 1 with the focal line and axis of rotation parallel to $\vec{N}_Y$ and the optical axis represented by $\vec{N}_Z$. The airborne absorber positioning approach (see Fig. 12) uses observation lines from the camera to the absorber tube center line situated in a reference plane E_{Ref} perpendicular to the focal line. Pairwise intersection of the observation lines delivers ΔX_{Abs} and ΔZ_{Abs}. Typically, the distance in longitudinal (Y-) direction between measurement positions is set to 0.5 m which delivers sufficient spatial resolution to describe the trend of absorber tube displacement.

The first step in the work flow is to determine the absorber tube edges in ROIs. Based on the cameras Interior Orientation (IOR) and spatial transformation information between each SCE and the corresponding Exterior Orientation (EOR), a grid of 3D coordinates $\vec{x}_{ROI}$ is projected onto the image to obtain an ortho-image (Fig. 11). The grid $\vec{x}_{ROI}$ is located in a plane fulfilling Eq. (4):

$$E_{ROI} : (\vec{x}_{ROI} - \vec{p}_{ROI}) \cdot \vec{n}_{ROI} = 0 \qquad (4)$$

where p_{ROI} is the vector to the current measurement position along the focal line ($\vec{N}_Y$) and $\vec{n}_{ROI}$ is the normal vector of the plane E_{ROI}, defined by $\vec{N}_Y$ and the Line-of-Sight (LOS) between camera and measurement position:

$$\vec{n}_{ROI} = (\overrightarrow{LOS_{ideal}} \times \vec{N}_Y) \times \vec{N}_Y \qquad (5)$$

Within these ortho-images, the 2D deviation of tube from the focal line d_{ROI} is detected via edge filters and linear regression. Fig. 11 shows an example tube detection results.

The result of the image processing is used to define a new plane (see Fig. 13) containing the EOR and the detected tube position within E_{ROI}:

$$E_{Tube} : (\vec{x}_{Tube} - \overrightarrow{EOR}) \cdot (\overrightarrow{LOS_{meas}} \times \vec{N}_Y) = 0 \qquad (6)$$

with

$$\overrightarrow{LOS_{meas}} = (\overrightarrow{EOR} - \vec{p}_{Tube}) \qquad (7)$$

and

$$\vec{p}_{Tube} = \vec{p}_{ROI} + d_{ROI} * (\overrightarrow{LOS_{ideal}} \times \vec{N}_Y) \qquad (8)$$

The final step to obtain a single observation line is the intersection of E_{Tube} with a reference plane E_{Ref} (see Fig. 13) defined by:

$$E_{Ref} : (\vec{x}_{Ref} - \vec{p}_{ROI}) \cdot \vec{N}_Y = 0 \qquad (9)$$

M observation lines create a scattered distribution of

$$N = \sum_{k=1}^{k=M-1} k \qquad (10)$$

pairwise intersections XZ_{ij} within E_{Ref} (see Figs. 12 and 15). The tube position and its uncertainty can be derived from the mean value

$$\overline{Abs_{Meas}} = \frac{1}{N} \sum_{k=1}^{N} XZ_{ij} \qquad (11)$$

and the standard deviation

$$\sigma_{Abs_{Meas}} = \sqrt{\frac{1}{N-1} \sum_{k=1}^{N} (XZ_{ij} - \overline{Abs_{Meas}})^2}. \qquad (12)$$

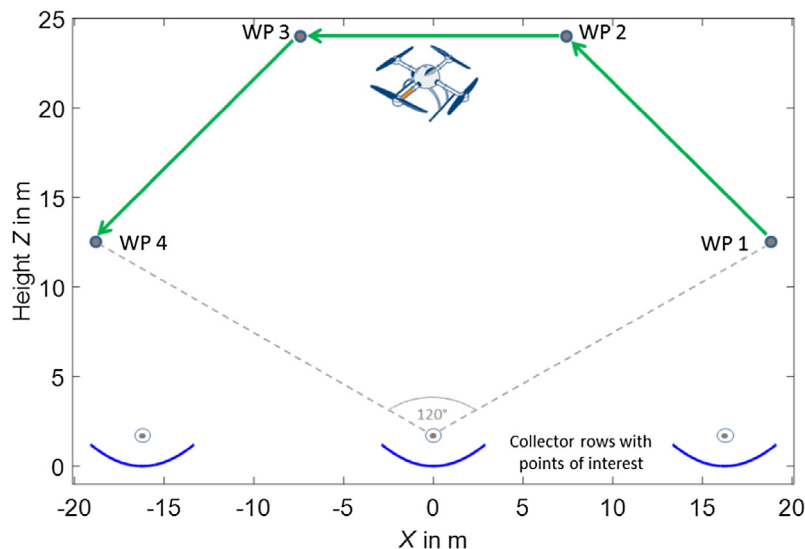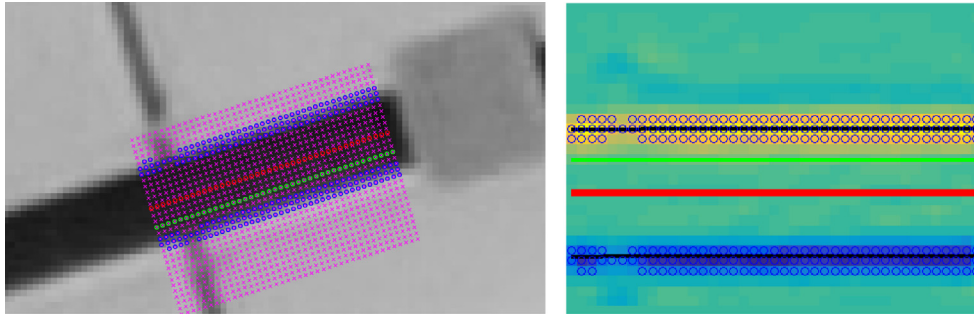Deviations from the focal line are obtained by

Fig. 10. Cross section perpendicular to the focal line showing the parabolic mirror with the WPs of each SCE flyover. Images for SD_X measurement are taken along path $\overline{WP2WP3}$, while additional images for the absorber positioning are taken along path $\overline{WP1WP2}$ and $\overline{WP3WP4}$.

Fig. 11. Edge based tube detection, reprojected in the original image (left) and within the ortho-image (right). Green markers denote the location of the ideal focal line, and red markers show the tube center deduced from linear intensity weighted regression on tube edge elements (blue circles). The vertical difference in the right image between ideal focal line and tube center is denoted as d_{ROI} (see Eq. (8)).
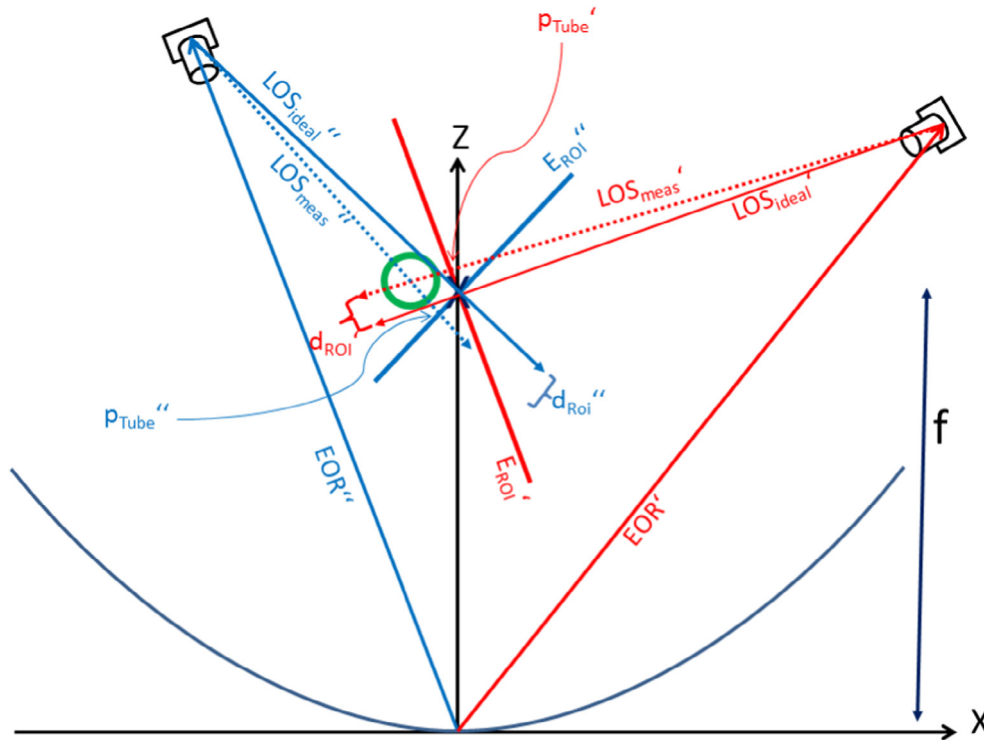
Fig. 12. Example cross section containing E_{Ref} to show the methodology of the absorber positioning, based on two observations. Planes E_{Tube} and E_{ROI} are represented by lines as they are always perpendicular to any XZ plane. E_{Tube} is displayed as LOS. The difference between ideal and measured tube position is denoted as d_{ROI}. Camera distances to the PTC are not drawn to scale in order to improve the presentation.

$$[\Delta X_{Abs}, \Delta Z_{Abs}] = \overline{Abs_{Meas}} - [0, f]$$

4.2. Uncertainty analysis

In the following section, statistic and systematic error sources are identified and evaluated for both the manual, photogrammetric benchmark measurement, and the airborne measurement. Uncertainty estimates and their contributions are given in Table 1.

#### 4.2.1. Uncertainty of photogrammetric benchmark measurement

Close range photogrammetry delivers 3D-coordinates with an absolute uncertainty <0.5 mm for a measurement volume containing a single SCE. The center of the glass envelope tube is calculated via circle fit of at least eight markers on the circumference. A conservative approach assigns an uncertainty in the same order to the glass tube center line ($\sigma_{Glass_{PG}} \approx 0.5$ mm). Systematic deviations

may arise due to misalignment between the rotation axis and the rest of the steel structure (see Section 3.1). Such deviation, which would lead to inconsistencies between benchmark and QFly measurement are prevented by ignoring the rotation axis coordinates in this case and by using the approach described in Section 4.1 (best fit of mirror coordinates to design values). The semi-automatic determination of the eccentricity of the steel- relative to the glass tube (see Section 3.3, and Fig. 7) is subject to blurring and weak contrast ($\sigma_{Abs_{Ecc}} \approx 1.0$ mm). The combined uncertainty in X and Z direction is determined according to $\sigma_{AbsXZ_{Bench}} \approx \sqrt{\sigma_{Glass_{PG}}^2 + \sigma_{Abs_{Ecc}}^2}$.

4.2.2. Uncertainty of airborne measurement

Uncertainties of the camera positioning (σ_{EOR}) and the image processing to derive the tube center displacement (d_{ROI}) cause a fairly wide distribution of the resulting intersection points (see
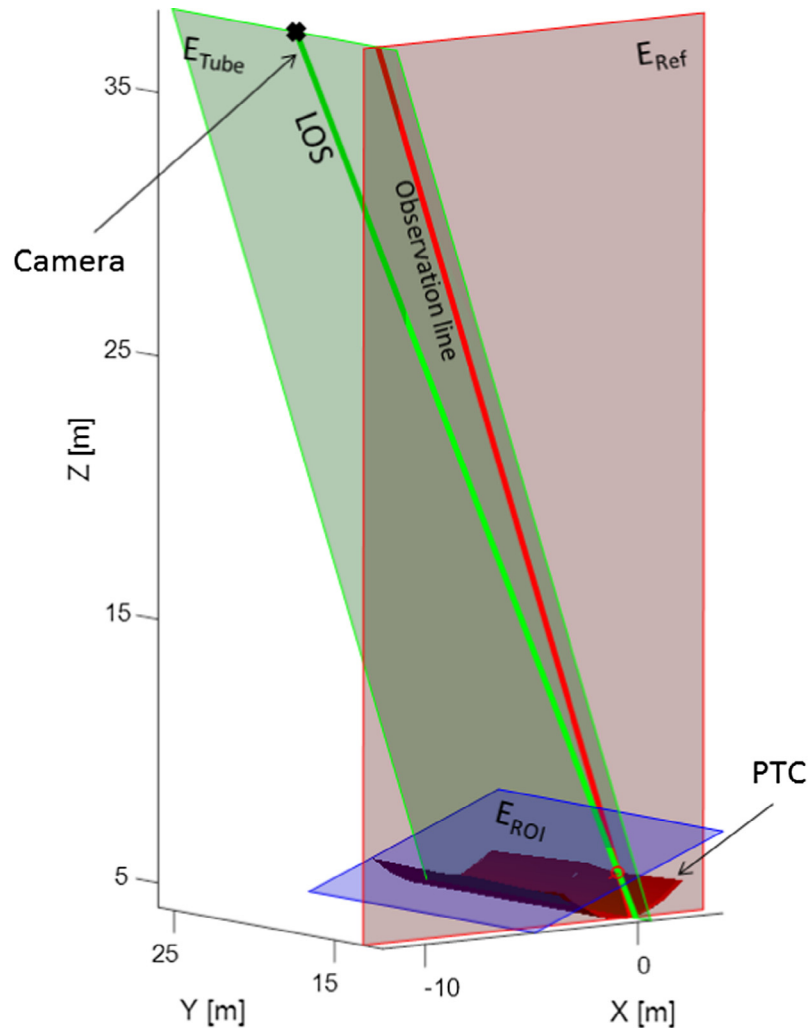
Fig. 13. 3D visualization of the planes applied to derive the absorber tube position in the ortho-image (see Fig. 11). Tube detection image processing is carried out inside a fraction of the blue plane E_{ROI} (see Eq. (4)). The resulting LOS (green line) in combination with camera position provides E_{Tube} (Eq. (6)) in green. The intersection of E_{Tube} with E_{Ref} (Eq. (9), red) delivers a single observation line (red).

Fig. 15). The contribution from the camera positioning can be estimated from values returned from the bundle adjustment. Typical camera position uncertainty of ($\sigma_{EOR} \approx 5.0$ mm) was also confirmed using a total station theodolite (Prahl et al., 2013, Section 5.1.1). The contribution from the image processing ($\sigma_{d_{ROI}} \approx 2.0$ mm) in the ortho image plane arises from blurring of the absorber edges and limited resolution (see Fig. 11). The expected uncertainty of one LOS in the focal line is $\sigma_{LOS} = \sqrt{\sigma_{EOR}^2 + \sigma_{d_{ROI}}^2}$. The uncertainty ellipsoid (see Fig. 14) provides the X and Z share of the single line-line intersection uncertainty. The ellipse shape is determined by the intersection angle of corresponding LOSs; least values are achieved for intersection angles of 90°.

The uncertainty of the airborne tube positioning is reduced by the large number N (see Eq. (10)) of pairwise line-line intersections to a value considerably lower than σ_{Abs}:

$$u_{Abs} = \frac{1}{\sqrt{N}} \cdot \sigma_{Abs} \qquad (13)$$

Estimated values (see Tables 1 and 2) are confirmed by the characteristics of the distribution of intersection points (see Fig. 15).

4.3. Validation

The validation of the airborne approach was carried out by measuring the HCE positions of three RP3 type SCEs with PG (benchmark) and QFly. HTF was circulated in the corresponding loop at constant temperature ($\simeq 50$ °C) during the whole measurement campaign in order to avoid any temperature change induced alteration of the HCE position. Any contradiction between PG and QFly measurement arising from time delay can be identified by comparing the two PG measurements before and after the QFly data acquisition (red and green symbols in Fig. 16). Spatial deviation between both approaches is compensated by interpolating the QFly results on the position of the benchmark measurement. For the benchmark, retro-reflective markers were attached to the axis of rotation, onto the mirror surface above the mirror attachment points of the support structure and on the glass envelope tube (see Fig. 7) of the PTC. Three positions per HCE are regarded a reasonable trade-off between spatial resolution and effort. Approx. 550 images were taken with standard equipment[5] and the photogrammetric evaluation was performed with commercial software.[6] The determination of glass envelope tube position and the eccentricity

---

[5] Nikon D300s digital SLR camera, ring flash Sunpak Auto 16R Pro.
[6] AICON DPA Pro.
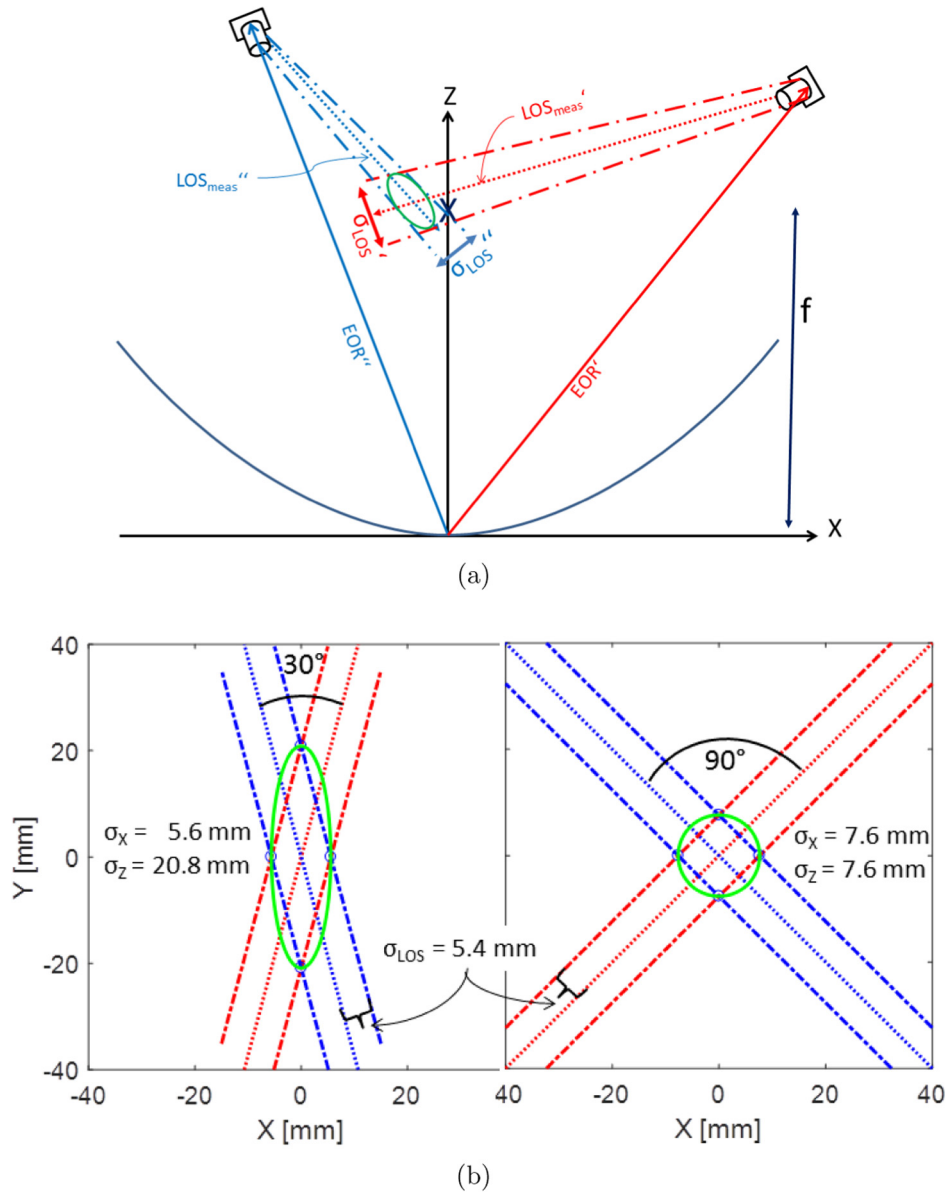
Fig. 14. (a) Cross section with intersection measurement error. Uncertainty of the camera position σ_{EOR} and the image processing $\sigma_{d_{ROI}}$ defines the spread of the LOS named σ_{LOS}. The shape of the uncertainty ellipse depends on the intersection angle an σ_{LOS} of each observation. Camera distances to the PTC are not drawn to scale in order to improve the presentation. (b) Examples for uncertainty ellipses for identical σ_{LOS} but different intersection angles of 30° and 90°.

of the steel tube within the glass envelope tube was carried out as described in Section 3.3. About 700 aerial images were captured for the QFly measurement. Most of the images serve to provide a stable configuration for the photogrammetric evaluation (bundle adjustment), which includes a simultaneously optimization of EOR, IOR, and object coordinates. For the absorber positioning, about 50 images captured along the individual flight route above each SCE (see Fig. 10) are used. ROIs are defined approx. ±150 mm along the focal line with respect to PG measurement locations, as the direct view on the glass tube is obstructed in that region by the PG markers. Fig. 16 shows the result of the comparisons between QFly and benchmark for the first of three investigated SCEs. Table 3 provides an overview on the statistics of deviations for all three SCEs.

The validation shows good agreement between benchmark and airborne measurement within the expected uncertainty margins for the benchmark ($\sigma_{AbsXZ_{Bench}} \simeq 1.2$ mm) and QFly ($u_{Abs} \simeq 0.2$ mm in X-direction and $u_{Abs} \simeq 0.6$ mm in Z-direction). Deviations are somewhat larger for SCE 1. The primary cause for this is a system-

atic off-set in the transformation onto the design data. Different POIs were used in either case.[7] The manually attached mirror markers have not been positioned with sufficient accuracy for SCE 1, while transformation parameters of SCE 2 and 3 suggest sufficient accuracy of the transformation parameters here. The uncertainty for the absorber tube deviation based on the newly developed airborne approach meets the accuracy requirements for the calculation of mirror shape deviations based on the TARMES approach ($\lesssim 2$ mm) and simulation of optical performance with numerical RT ($\lesssim 2$ mm). QFly also outperforms the benchmark measurement (PG in combination with evaluation of eccentricity images) and previous manual methods (hook rod in combination with evaluation of eccentricity images) in terms of measurement accuracy and effort.

---

[7] Mirror corners and gaps for QFly and manually attached markers for the PG measurement.
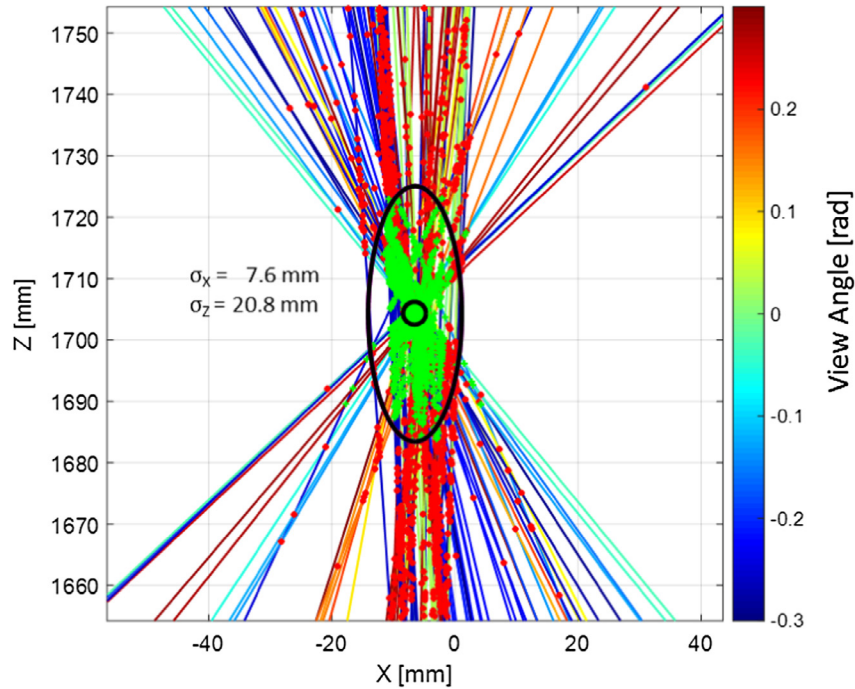
Fig. 15. Sample distribution of pairwise line-line intersections inside E_{Ref}. Outliers (red) are not used to calculate the tube position (small black circle). The main criterion for outliers is the intra-line intersection angle (min. 10°). Line colors correspond to the angle [rad] between the LOS and E_{Ref}, however this parameter does not affect the accuracy. Typical standard deviations for the detected tube position are in the range of 7.6 mm in X-Direction and 20.8 mm in direction of the optical axis, in accordance with the ellipse (black) obtained from theoretical uncertainty estimations.

Table 1
Uncertainty estimates for photogrammetric benchmark coordinates and LOS QFly measurement as described in Sections 4.2.1 and 4.2.2. Derivation of final QFly measurement uncertainty is given in Table 2.

Benchmark		QFly	
Param	Value	Param	Value
$\sigma_{Glass_{PG}}$ [mm]	$\simeq 0.5$	σ_{EOR} [mm]	$\simeq 5.0$
$\sigma_{Abs_{Ecc}}$ [mm]	$\simeq 1.0$	$\sigma_{d_{ROI}}$ [mm]	$\simeq 2.0$
$\sigma_{AbsXZ_{Bench}}$ [mm]	$\simeq 1.2$	σ_{LOS} [mm]	$\simeq 5.4$

Table 2
Uncertainty estimates for QFly absorber tube coordinates.

| Parameter	Direction	
	X	Z
σ_{Abs} [mm]	7.6	20.8
M	≈ 50	≈ 50
u_{Abs} [mm]	0.21	0.59

5. Summary and outlook

Various effects during construction and operation of the solar field may influence the geometry of PTC collectors, in particular the position of the absorber tube relative the concentrators focal line. Knowledge about the absorber tube position in different operation conditions is necessary for prediction and optimization of the optical performance, since exceeding the narrow tolerance range will diminish solar plant performance. Various manual, ground based methods to access the absorber tube position exist, but these methods show limited suitability for the characterization of the large number of SCEs used in commercial power plants. An exception is the coupling of sample measures with statistical methods as described in Zhu and Turchi (2017). We present an airborne approach, which delivers mirror shape and absorber tube position with an integrated, airborne measurement system. The accuracy of the airborne absorber tube positioning has been validated under real solar field conditions for a total HCE length of 36 m, showing an accuracy below 1.5 mm for each lateral- and height absorber tube deviation.

This accuracy fulfills the requirement for Ray Tracing based performance predictions, retroactive alignment and especially for mirror shape measurements based on the distant observer approach. The measurement effort for the complete airborne geometric characterization for an entire ET SCA with 12 SCEs is about 2 h for preparation and data acquisition, and another 3 h for fully automatic evaluation, which is about a factor of 10 faster than previous manual methods. QFly thus enhances significantly the accessibility of geometric data relevant for the optical performance. However, the characterization of entire solar fields with $\simeq 600$ SCAs is still beyond the scope of this method. The fast geometric characterization of entire solar fields within less than one day (data acquisition only) is subject to current developments using airborne images from considerably higher flight altitudes.

Planned improvements of the presented method aim at avoiding completely the use of artificial coded targets, by deploying image registration in time series of un-interrupted image acquisition. This would further reduce effort and required manpower though distribution and collection of the coded targets account for 70% of the measurement effort. The commercial applications of airborne absorber tube displacement is mainly motivated by performance evaluation. It can also be useful to identify and predict REPA-failure, as increased REPA-friction provides a characteristic ΔX_{Abs}-pattern towards the end of the affected SCA.
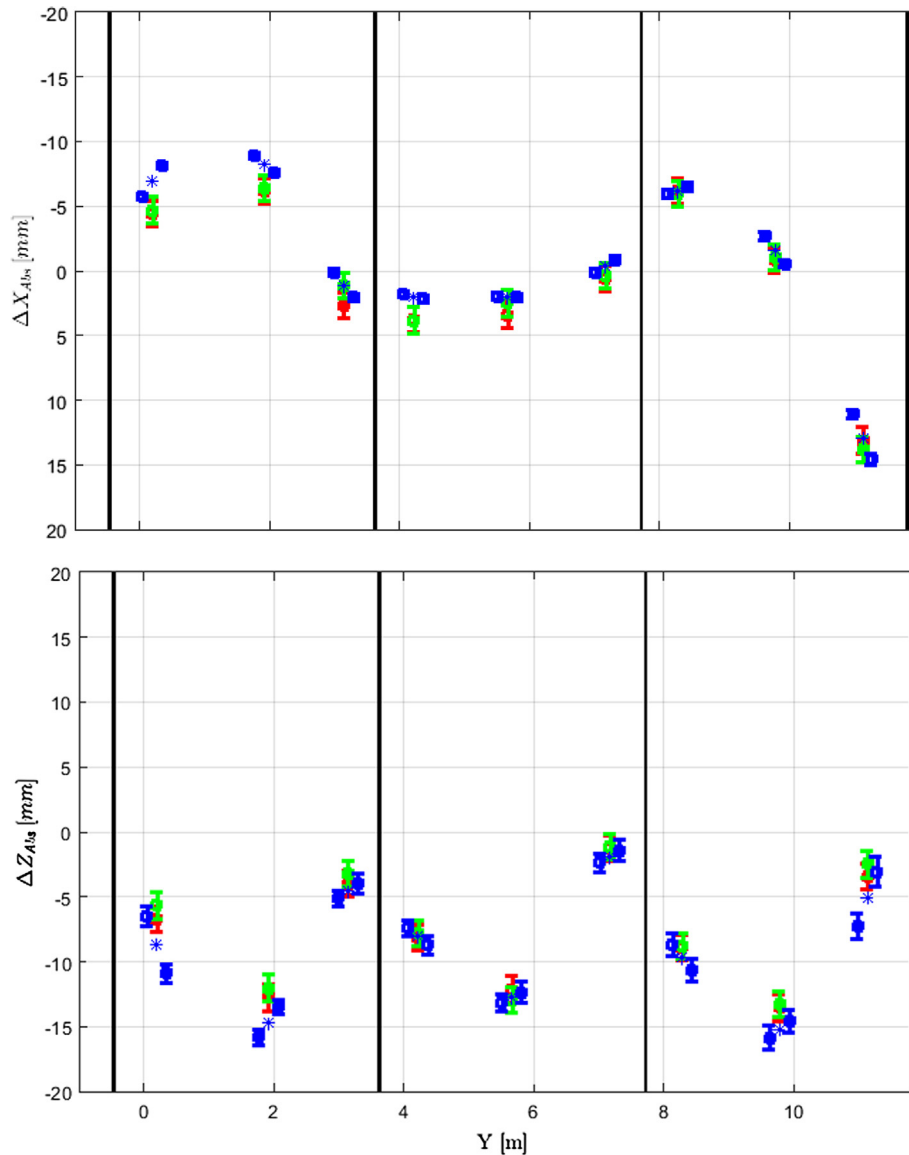
Fig. 16. Comparison of absorber tube position for the first of three SCEs by QFly (blue), and PG before (red) and after (green) the QFly measurement. The photogrammetric benchmarks before and after the airborne data acquisition are consistent. Interpolated QFly results between data points enclosing the benchmark measurement are represented by blue symbols (∗). The characteristics of the ΔX_{Abs} (upper) and ΔZ_{Abs} (lower) match well within the expected uncertainty margins. Rather large deflections are due to the fact that data has been acquired from first generation ET collectors within the boiling section of a DSG boiler, where large deflections due to thermal stress are visible.

Table 3
Statistics of the difference between QFly and PG reference measurement. Expected uncertainties for benchmark- and airborne measurement can be found in Tables 1 and 2.

	RMS [mm]			Mean [mm]		
	X	Z	XZ	X	Z	XZ
SCE1	1.32	1.55	2.04	1.13	1.28	1.85
SCE2	0.92	0.93	1.30	0.47	0.55	0.99
SCE3	0.98	0.82	1.28	−0.86	0.37	1.16

References

Almanza, R., Lentz, A., Jimenez, G., 1997. Receiver behavior in direct steam generation with parabolic troughs. Sol. Energy 61 (4), 275–278.

Belhomme, B., Pitz-Paal, R., Schwarzbözl, P., Ulmer, S., 2009. A new fast ray tracing tool for high-precision simulation of heliostat fields. J. Sol. Energy Eng., 131

Bendt, P., Rabl, A., Gaul, H., Reed, K., 1979. Optical Analysis and Optimization of Line Focus Solar Collectors. Technical Report. Solar Energy Research Institute, Golden, Colorado (USA) <www.nrel.gov/docs/legosti/old/092.pdf> (retrieved 2015.03.24).

Binotti, M., Zhu, G., Gray, A., Manzolini, G., 2012. An Analytical Approach Treating Three-dimensional Geometrical Effects of Parabolic Trough Collectors. Technical Report. NREL/CP-5500-54712.

Bode, S.-J., Gauche, P., 2012. Review of optical software for use in concentrating solar power systems. In: Proceedings Southern African Solar Energy Conference. <sun.ac.za/sterg/files/2012/06/CSP-06.pdf> (retrieved 2015.03.24).

Bouguet, J., 2010. Camera Calibration Toolbox for Matlab. <http://www.vision.caltech.edu/bouguetj/calib_doc/> (retrieved 2015.03.24).

Buck, R., 2010. Solar Power Raytracing Tool Spray User Manual Ver. 17. Technical Report. DLR e.V.

Buie, D., Monger, A., 2004. The effect of circumsolar radiation on a solar concentrating system. Sol. Energy 76. Solar World Congress 2001.

Burkholder, F., Kutscher, C.F., 2009. Heat Loss Testing of Schott's 2008 PTR70 Parabolic Trough Receiver. National Renewable Energy Laboratory.

CSP-Today 2017. CSP Today Global Tracker. <http://social.csptoday.com/tracker/projects> (retrieved 2017.04.26).

Diver, R.B., Moss, T.A., 2007. Practical field alignment of parabolic trough solar concentrators. J. Sol. Energy Eng. 129 (2), 153–159.

Fernandez-Garcia, A., Zarza, E., Valenzuela, L., Perez, M., 2010. Parabolic-trough solar collectors and their applications. Renew. Sustain. Energy Rev. 14 (7), 1695–1721.

Fernandez-Reche, J., Valenzuela, L., 2012. Geometrical assessment of solar concentrators using close-range photogrammetry. Energy Procedia 30 (0), 84–90. 1st International Conference on Solar Heating and Cooling for Buildings and Industry (SHC 2012).

Francini, F., Fontani, D., Sansoni, P., Mercatelli, L., Sani, D.J.E., 2012. Evaluation of surface slope irregularity in linear parabolic solar collectors. Int. J. Photoenergy, 2012.

Garcis, S., Bello-Garcia, A., Ordonez, C., 2012. Estimating intercept factor of a parabolic solar trough collector with new supporting structure using off-the-shelf photogrammetric equipment. Appl. Energy 92, 815–821.

Geyer, M., Lüpfert, E., Osuna, R., Esteban, A., Schiel, W., Zarza, A.S.E., Nava, P., Langenkamp, J., Mandelberg, E., 2002. EUROTROUGH-parabolic trough collector developed for cost efficient solar power generation. In: Proceedings of the 11th SolarPACES Conference, September 2002, Zurich, Switzerland, pp. 04–06.

Gonzalez, R.C., Woods, R.E., Eddins, S.L., 2004. Digital Image Processing Using MATLAB. Pearson Education India.

Heller, P., Meyer-Grünefeldt, M., Ebert, M., Jannote, N., Nouri, B., Pottler, K., Prahl, C., Reinalter, W., Zarza, E., 2011. KONTAS–a rotary test bench for standardized qualification of parabolic trough components. In: Proceedings of the 17th SolarPACES Conference, 20–23 September 2011, Granada, Spain.

Hirsch, T., Ebert, M., Eck, M., Eickhoff, M., Janotte, N., Keller, L., Meyen, S., Meyer-Grünefeld, M., Munini, M., Nanz, L., Prahl, C., Röger, M., Wittmann, M., 2012. Stratified flow phenomena in parabolic trough systems. In: Proceedings of the 18th SolarPACES Conference, 11–14 September 2012, Marrakech, Morocco.

Ho, C.K., 2008. Software and Codes for Analysis of Concentrating Solar Power Technologies. Technical Report. Sandia National Laboratories. <http://energy.sandia.gov/wp/wp-content/gallery/uploads/SAND2008-8053.pdf> (retrieved 2014-07-16).

Irena, 2013. Concentrating Solar Power – Technology Brief. Technical Report. International Renewable Energy Agency.

Iverson, B.D., Flueckiger, S.M., Ehrhart, B.D., 2011. Trough heat collection element deformation and solar intercept impact. In: Proceedings of the 17th SolarPACES Conference, 20–23 September 2011, Granada, Spain.

Jorgensen, G., Burkholder, F., Gray, A., Wendelin, T., 2009. Assess the Efficacy of an Aerial Distant Observer Tool Capable of Rapid Analysis of Large Sections of Collector Fields. Technical Report NREL/MP-550-44332. NREL.

Khanna, S., Kedare, S.B., Singh, S., 2013. Analytical expression for circumferential and axial distribution of absorbed flux on a bent absorber tube of solar parabolic trough concentrator. Sol. Energy 92 (0), 26–40.

Khanna, S., Kedare, S.B., Singh, S., 2014. Deflection and stresses in absorber tube of solar parabolic trough due to circumferential and axial flux variations on absorber tube supported at multiple points. Sol. Energy 99 (0), 134–151.

Khanna, S., Singh, S., Kedare, S.B., 2015. Explicit expressions for temperature distribution and deflection in absorber tube of solar parabolic trough concentrator. Sol. Energy 114 (0), 289–302.

Luhmann, T., Robson, S., Kyle, S., Harley, I., 2006. Close Range photogrammetry: Principles, Techniques and Applications. Whittles Publishing.

Lüpfert, E., Pottler, K., Ulmer, S., Riffelmann, K.-J., Neumann, A., Schiricke, B., 2007. Parabolic trough optical performance analysis techniques. J. Sol. Energy Eng. 129 (2), 147–152.

Mousazadeh, H., Keyhani, A., Javadi, A., Mobli, H., Abrinia, K., Sharifi, A., 2009. A review of principle and sun-tracking methods for maximizing solar systems output. Renew. Sustain. Energy Rev. 13 (8), 1800–1818.

Nouri, B., 2014. Thermal Test at the KONTAS Facility. Unpublished data.

Pottler, K., Lüpfert, E., Johnston, G.H., Shortis, M.R., 2004. Photogrammetry: a powerful tool for geometric analysis of solar concentrators and their components. In: ASME 2004 International Solar Energy Conference. American Society of Mechanical Engineers, pp. 719–726.

Pottler, K., Ulmer, S., Lüpfert, E., Landmann, M., Röger, M., Prahl, C., 2014. Ensuring performance by geometric quality control and specifications for parabolic trough solar fields. Energy Procedia 49 (0), 2170–2179. Proceedings of the SolarPACES 2013 International Conference.

Prahl, C., Stanicki, B., Hilgert, C., Ulmer, S., Röger, M., 2011. Airborne shape measurement of parabolic trough collector fields. In: Proceedings of the 17th SolarPACES Conference, 20–23 September 2011, Granada, Spain.

Prahl, C., Stanicki, B., Hilgert, C., Ulmer, S., Röger, M., 2013. Airborne shape measurement of parabolic trough collector fields. Sol. Energy 91 (0), 68–78.

Price, H., Lupfert, E., Kearney, D., Zarza, E., Cohen, G., Gee, R., Mahoney, R., 2002. Advances in parabolic trough solar power technology. J. Sol. Energy Eng. 124 (2), 109–125.

Ren, L., 2014. A review of available methods for the alignment of mirror facets of solar concentrator in solar thermal power system. Renew. Sustain. Energy Rev. 32 (0), 76–83.

Schiricke, B., 2008. Optischer Wirkungsgrad von Parabolrinnenkollektoren: Modellierung und Messung (PhD thesis). RWTH Aachen.

Schott, 2015a. SCHOTT PTR70 4th Generation Datasheet.

Schott, 2015b. Setting the Benchmark in Receiver Technology. Technical Report. SCHOTT Solar CSP GmbH (accessed 31-March-2015).

Stanicki, B., 2011. Validierung eines messsystems zur vermessung von parabolrinnenkollektoren aus der luft (Master's thesis). Hochschule Ravensburg Weingarten. Contact/Request Dokument: christoph.prahl@dlr.de.

Stynes, J.K., Ihas, B., 2012a. Slope error measurement tool for solar parabolic trough collectors. In: World Renewable Energy Forum, Denver, Colorado. NREL/CP-5500-54636.

Stynes, K., Ihas, B., 2012b. Absorber alignment measurement tool for solar parabolic trough collectors. In: ASME 2012 6th International Conference on Energy Sustainability collocated with the ASME 2012 10th International Conference on Fuel Cell Science and Engineering and Technology. American Society of Mechanical Engineers, pp. 437–447.

Ulmer, Steffen, Heinz, Boris, Pottler, Klaus, Lüupfert, Eckhard, 2009. Slope error measurements of parabolic troughs using the reflected image of the absorber tube. J. Sol. Energy Eng. 131 (1), 011014.

Valdes, A., Almanza, R., Soria, A., 2014. Determining the deflection magnitude of a steel receiver from a {DSG} parabolic trough concentrator under stratified flow conditions. Energy Procedia 57 (0), 341–350. 2013 {ISES} Solar World Congress.

Vignarooban, K., Xu, X., Arvay, A., Hsu, K., Kannan, A., 2015. Heat transfer fluids for concentrating solar power systems–a review. Appl. Energy 146, 383–396.

Wood, R., 1981. Distant Observer Techniques for Verification of Solar Concentrator Optical Geometry. Technical Report. Technical Report UCRL-53220 and Lawrence Livermore National Laboratory.

WorldBank, 2010. MENA Assessment of the Local Manufacturing Potential for Concentrated Solar Power (CSP) Projects (Technical Report). World Bank Group. <http://www.cspworld.org/resources/mena-assessment-local-manufacturing-potential-concentrated-solar-power-csp-projects> (downloaded 2015-03-30).

Wu, Z., Lei, D., Yuan, G., Shao, J., Zhang, Y., Wang, Z., 2014. Structural reliability analysis of parabolic trough receivers. Appl. Energy 123 (0), 232–241.

Yaghoubi, M., Akbarimoosavi, S.M., 2011. Three dimensional thermal expansion analysis of an absorber tube in a parabolic trough collector. In: Proceedings of the 17th SolarPACES Conference, 20–23 September 2011, Granada, Spain.

Zhu, G., Lewandowski, A., 2012. A new optical evaluation approach for parabolic trough collectors: first-principle optical intercept calculation. J. Sol. Energy Eng. 134 (4), 041005.

Zhu, G., Turchi, C., 2017. Solar field optical characterization at stillwater geothermal/solar hybrid plant 2. J. Sol. Energy Eng. 139. 031002–031002-10.